Volume 17
Number 39
21 October 2025
Pages 22551-23186

Nanoscale

rsc.li/nanoscale

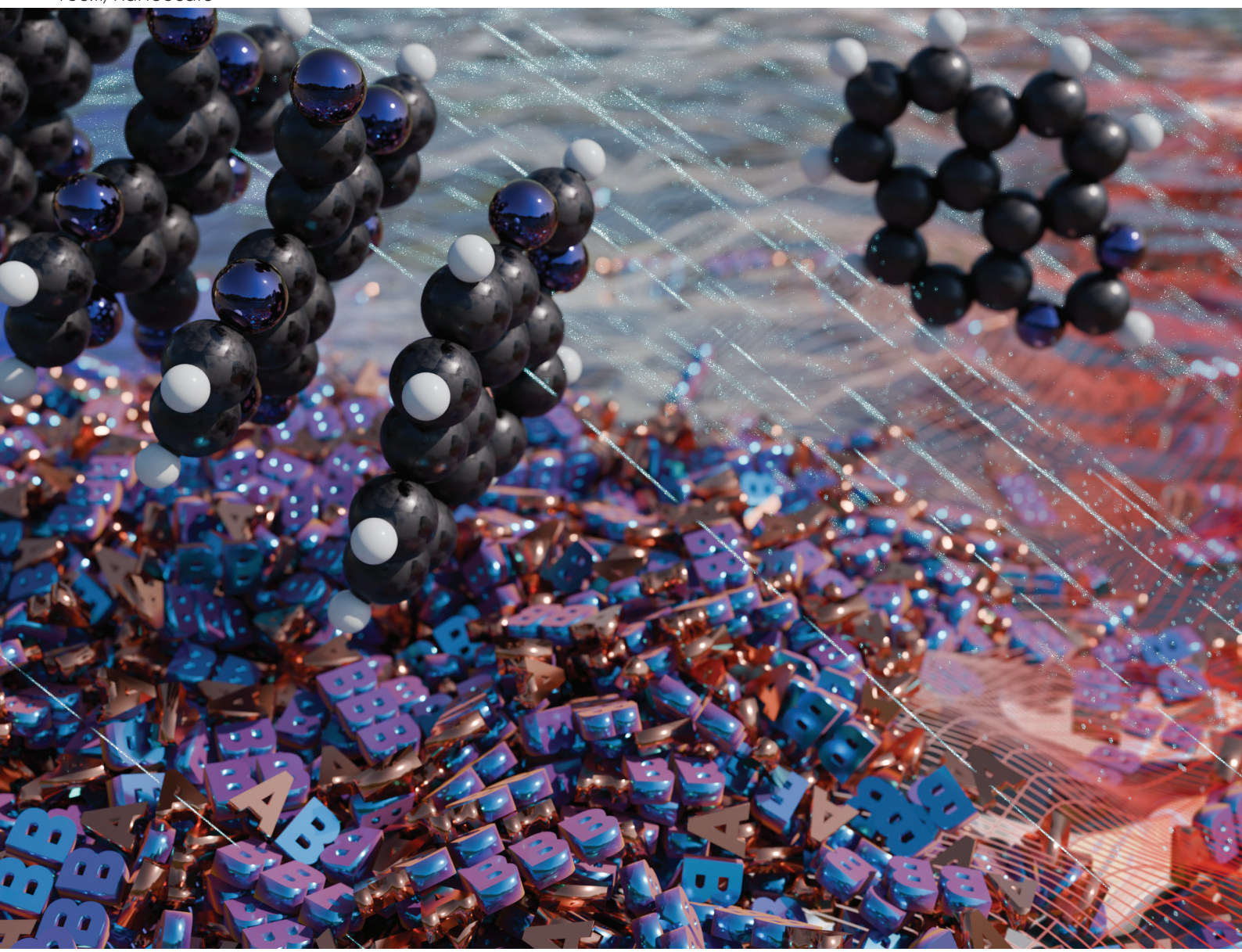

ISSN 2040-3372

ROYAL SOCIETY OF CHEMISTRY

PAPER

Michal Otyepka, Miroslav Medveď *et al.*
Computational design of donor–acceptor stacked polycyclic aromatic hydrocarbons as photocatalytic sites in carbon dots

NCNST

Nanoscale

PAPER

View Article Online
View Journal | View Issue

Cite this: *Nanoscale*, 2025, **17**, 22834

Computational design of donor–acceptor stacked polycyclic aromatic hydrocarbons as photocatalytic sites in carbon dots

Tomáš Hrivnák,[a,b] Martin Pykal,[c] Andrey L. Rogach,[a,d] Michal Otyepka *[a,c] and Miroslav Medved' *[c,e]

Carbon dots (CDs) are complex carbon-based nanomaterials with exceptional photoluminescence characteristics and great promise for sustainable metal-free photocatalysis. However, their structural heterogeneity poses a major challenge for the rational design and prediction of photocatalytic performance. To overcome this limitation, we propose a bottom-up strategy centered on CD-inspired systems with well-defined molecular architecture. Specifically, we computationally screened 5700 stacked polycyclic aromatic hydrocarbon aggregates, as representatives of CD aromatic domains, to identify donor–acceptor pairs capable of efficient charge separation under photoexcitation. Using a few carefully chosen molecular descriptors and a computationally efficient protocol, we identified best candidate systems for oxidative and reductive quenching pathways. Subsequent time-dependent density functional theory analysis confirmed that these systems exhibit key photocatalytic features: a charge-transfer character in the lowest excited state, well-separated bright local excitations, favorable redox potentials, and propensity for extended aggregation with core-surface charge separation. Our approach not only offers a practical design route for CD-like photocatalysts but also provides the fundamental understanding needed to engineer tunable, efficient, and sustainable donor–acceptor photocatalytic systems.

Received 22nd May 2025,
Accepted 28th August 2025

DOI: 10.1039/d5nr02170g

rsc.li/nanoscale

1. Introduction

Carbon dots (CDs) have emerged as compelling photoluminescent nanomaterials exhibiting many attractive features such as biocompatibility, low toxicity, and excellent water dispersability.[1,2] In addition, they can easily be prepared either by top-down approaches from various carbon sources (*e.g.*, graphene or carbon soot), using accessible molecular precursors or *via* biomass processing,[3,4] rendering them both cost-effective and environmentally friendly. Although the most exploited property of CDs is their intense and tunable photoluminescence,[5–7] in some cases, the photoexcitation of CDs can lead to the generation of charge-separated spin-active species, *i.e.* electrons and holes (e^-/h^+), thus forming oxidative or reductive sites exploitable as photocatalysts (PCs).[8,9] The size and composition of CDs can vary widely depending on the choice of precursors, reaction conditions, post-synthetic functionalization, and environmental factors,[3,10] which enables devising CDs with tailored photophysical properties. This also holds promise for designing PCs with finely tunable redox characteristics, thus opening a pathway towards highly efficient, selective, profitable and sustainable catalysis. A major challenge that still hampers the coherent rational design of CDs for light-emitting and photocatalytic applications is the complex multicomponent arrangement of CDs,[11–14] which can hardly be resolved at the atomistic level by current experimental techniques.

The intricate character of photoluminescence of CDs, usually involving both excitation-dependent and excitation-independent components with multi-exponential decays as well as the formation of charge-separated spin-active species in some CDs, strongly suggests that they contain multiple chromophoric centers that effectively communicate with each other upon CD photoexcitation.[15] Although the exact structure of these centers has not yet been fully resolved, there is strong

[a]*IT4Innovations, VSB – Technical University of Ostrava, 17. listopadu 2172/15, 708 00 Ostrava Poruba, Czech Republic*
[b]*Polymer Institute, Slovak Academy of Sciences, Dúbravská cesta 9, 845 41 Bratislava, Slovakia*
[c]*Regional Centre of Advanced Technologies and Materials, Czech Advanced Technology and Research Institute (CATRIN), Palacký University, Šlechtitelů 241/27, Olomouc, 783 71, Czech Republic. E-mail: michal.otyepka@upol.cz, miroslav.medved@upol.cz*
[d]*Department of Materials Science and Engineering, and Center for Functional Photonics (CFP), City University of Hong Kong, 83 Tat Chee Avenue, Kowloon, Hong Kong SAR, 999077, China*
[e]*Department of Chemistry, Faculty of Natural Sciences, Matej Bel University, Tajovského 40, 974 01 Banská Bystrica, Slovak Republic*

experimental evidence on their chemical nature. The highly intense excitation-independent photoluminescence component has been associated with the formation of small molecular fluorophores.[16–20] On the other hand, the changes in absorption and photoluminescence spectra occurring during a carbonization phase of CD formation have been attributed to the emergence of extended π-conjugated aromatic domains,[21–23] which can contain heteroatoms and various chemical functional groups. Specifically, polycyclic aromatic hydrocarbons (PAHs) of variable sizes, doping patterns and functionalization have been suggested as viable models of those aromatic domains in CDs, providing important insights into CD behavior.[24–32] For instance, Fu *et al.*[31] showed that a mixture of polymer-embedded PAHs (anthracene, pyrene and perylene) can mimic the optical excitation and emission characteristics of CDs. Moreover, an ensemble of functionalized N-doped PAHs of variable sizes was successfully employed to consistently describe both the photoluminescence behavior and the generation of electron–hole pairs in catalytically active L-aspartic acid-based CDs.[33]

In this study, we follow a similar design strategy with the aim to propose structurally well-defined functionalized N-doped PAH-based complexes, enabling the formation of long-living charge-separated excited states in CDs critical for photocatalysis. To screen a large number of PAH complexes, we introduce a computationally efficient selection procedure based on relevant single molecular descriptors followed by a more detailed analysis of the best candidates using time-dependent density functional theory (TD-DFT) methodology. We also carefully investigate aggregation preferences and optical properties of complexes composed of four selected PAH species in order to devise CD-like systems, featuring a core–shell arrangement with the separated e^-/h^+ pair in their lowest excited state. Subsequently, the performance of individual stacked PAH aggregates is reflected upon considering monomer descriptors and structural arrangements to further elucidate the underlying effects driving their optical and redox properties. The general ability of the proposed procedure to screen for stacked donor–acceptor complexes with tunable characteristics is scrutinized and validated.

2. Methods

Design strategy

PAH aggregates can act as potential PCs following either oxidative quenching or reductive quenching mechanisms[34] (Fig. 1). Based on the preferred pathway, we will distinguish between OxQ and RedQ systems, respectively. In the former, the photo-excited PC (OxQ*) rapidly relaxes into a low-lying charge transfer (CT) state with increased electron density in an outer region of the system. Such a site can function as an electron donor to species in its vicinity, which are either substrate (SUB) or sacrificial acceptor (SA) molecules. The oxidized cationic form (OxQ^+) is then reduced back to the neutral state during the dark reaction. The SUB can also enter the cycle in this stage, resulting in its oxidation in the dark process. In the case of the RedQ mechanism, the photo-excitation of the PC leads to electron transfer into the inner region creating a hole at the shell. Photoexcited RedQ* species can thus serve as electron acceptors. The requirements for a specific PC may substantially differ depending on the quenching pathway and the nature of the SUB system. From a thermodynamic point of view, this imposes criteria on the ordering of the standard redox potentials ($E°$) of respective half-reactions. For example, in the case of the oxidative quenching mechanism involving SUB reduction and a sacrificial donor (SD) for the $OxQ^+ \rightarrow$ OxQ regeneration process, it is required that $E°(OxQ^+/OxQ^*) < E°(SUB/SUB^-) < E°(SD^+/SD) < E°(OxQ^+/OxQ)$. The individual redox potentials can be approximated by respective electron affinities (EAs) and ionization potentials (IPs) of the species in their ground state (GS) and – in the case of OxQs – also in their excited state (ES). For an ideal PC, the IP/EA* and EA/IP* values should straddle the reduction and oxidation potentials of the other systems involved in the photocatalytic process,[35,36] with EA* and IP* denoting the respective properties in ES. Although the criteria on the individual redox potentials ensure thermodynamic feasibility of the photocatalytic cycle, other characteristics such as efficient light absorption, a long enough half-life of the charge separated state, and the accessibility of the active site for the activation and the release of involved species also need to be considered in practical applications. Graphitic carbon nitride ($g\text{-}C_3N_4$) is an exemplary case, which fulfills thermodynamic requirements for the water-splitting reaction even in a pristine form, but requires further modifications[37,38] for boosting its photocatalytic activity.

Our design strategy for the identification of functioning OxQ/RedQ dimer pairs involves multiple steps (Scheme 1). First, key molecular descriptors of isolated monomers are utilized to identify complementary stacked PAH pairs presumably featuring the significant charge-transfer (CT) characteristic of their lowest singlet excited state (S_1). Descriptors ensuring this requirement are the energies of the highest occupied molecular orbital (HOMO) and the lowest unoccupied molecular orbital (LUMO) of the two individual components. We label the donor and acceptor subsystems of such a CT state as **A** and **B**, respectively. The required energy order of the frontier molecular orbitals (MOs) is $E_{LUMO(A)} > E_{LUMO(B)} > E_{HOMO(A)} > E_{HOMO(B)}$ (Fig. 1c). Ideally, the ^{1}CT state should be long-living, *i.e.*, featuring a sufficiently high vertical excitation energy and low oscillator strength (f) to decrease the probability of (non) radiative decay pathways, or able to efficiently transform into a triplet state (^{3}CT) *via* an intersystem crossing (ISC) event. The ^{1}CT state is presumably formed *via* internal conversion(s) of a bright local excitation (LE) in **A**. Irrespective of the type of quenching, these characteristics of the CT and LE states impose further criteria for the selection of suitable PAH pairs:

(1) The difference between $E_{HOMO(A)}$ and $E_{HOMO(B)}$ should be high enough to ensure sufficiently pure CT state (with a hole created on **A**) with low oscillator strength, resulting from weak spatial overlap of HOMO and LUMO in the complex;

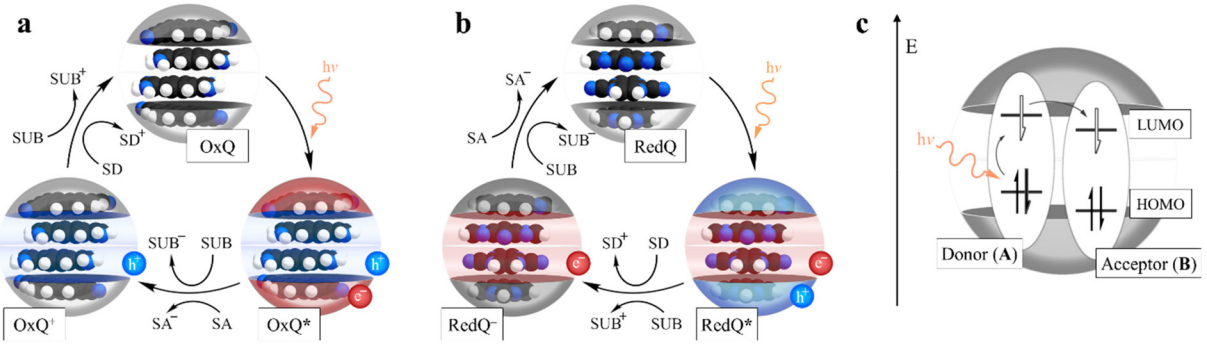

Fig. 1 (a) Oxidative quenching mechanism with the photo-excited OxQ* system serving as the electron donor in the bright phase of the cycle with subsequent regeneration from OxQ^+ in the dark phase. (b) Reductive quenching mechanism with the photo-excited RedQ* system acting as an electron acceptor in the bright phase with subsequent regeneration from $RedQ^-$ in the dark phase. SUB, SD, SA stand for substrate, sacrificial donor and sacrificial acceptor, respectively. (c) Molecular orbital (MO) representation of the **AB** complex and formation of an exciplex characterized by intermolecular CT produced *via* internal conversion following a local excitation (LE) of **A**.

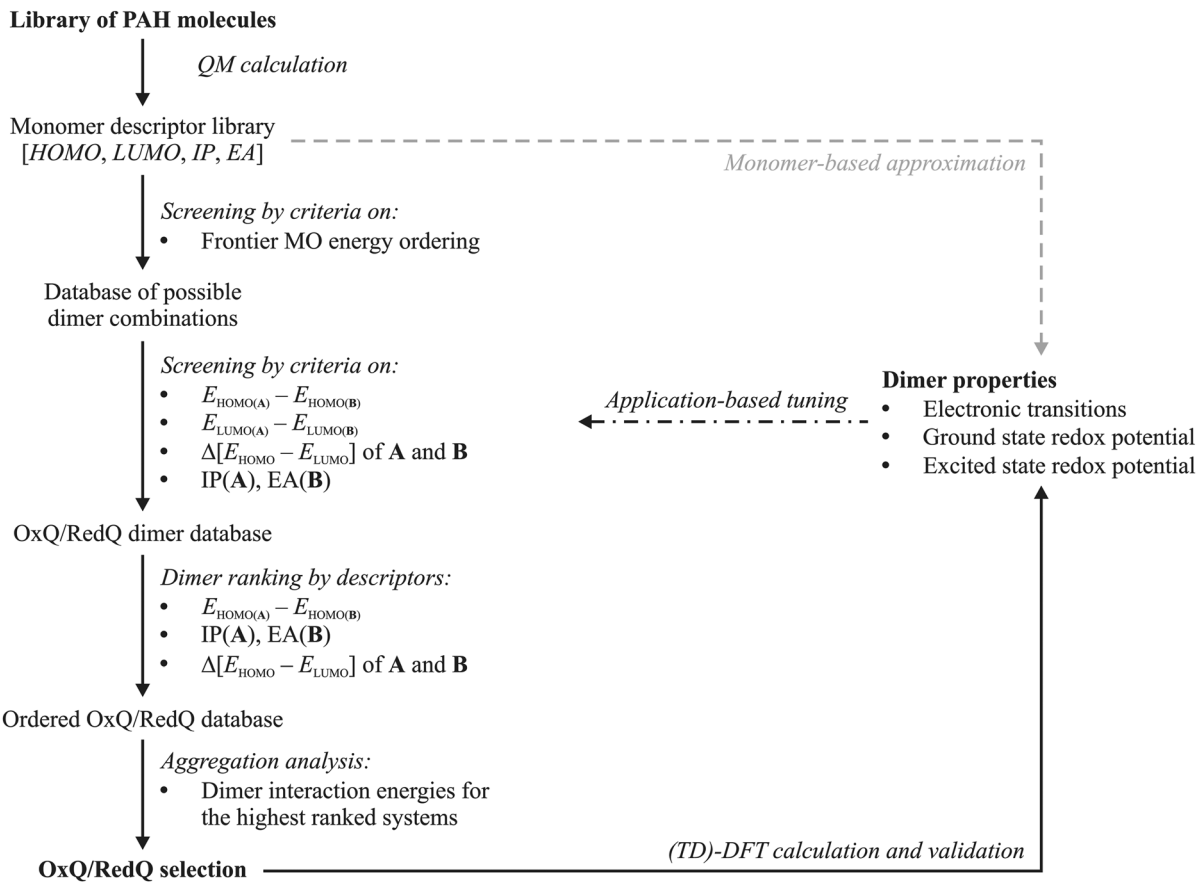

Scheme 1 Stepwise schematic representation of the applied design strategy for the identification of functioning OxQ/RedQ dimer pairs. Initial library of PAH molecules is subject to a series of screening and ordering procedures to obtain a smaller selection of the best performing OxQ and RedQ systems. These are then subject to aggregation analysis and, finally, TD-DFT property validation for dimers and extended tetramer systems. Approximate property evaluation based on monomer descriptors is also available and discussed.

(2) The difference between the E_{HOMO}–E_{LUMO} gaps of **A** and **B** should be large enough to allow for an addressable LE of **A** featuring high oscillator strength, *i.e.* high absorptivity of the **AB** complex;

(3) The $E_{LUMO(A)}$–$E_{LUMO(B)}$ gap should be >0.3 eV to attain a CT state with e^- localized on **B**, as a commonly assumed empirical lower limit for efficient charge separation of the donor–acceptor pair in studies of organic solar cells,[39–44]

although the value was subject to debate[45,46] and would require further validation for a wider range of donor–acceptor complexes;

(4) the IP(**A**)–EA(**B**) difference should be tentatively >2.0 eV, so that the vertical excitation energy of the CT state was sufficiently large to avoid a non-radiative decay.

In addition, the **AB*** complex needs to be effectively quenched by donating a hole or an electron to SUB/SA/SD in oxidative quenching or reductive quenching processes, respectively. The plausibility of a redox reaction between **AB*** and SUB/SA/SD can be qualitatively assessed in terms of adiabatic IP and EA values of **A** and **B**, which include the MO relaxation in the subsystems accompanying the formation of the CT state. Therefore, two additional descriptors for selecting suitable PAH pairs were introduced. For OxQs, it is desirable to keep IP(**A**) and EA(**B**) low enough to achieve sufficient stability of the hole on **A** and high reductive potential of **B**, respectively. Reverse requirements, *i.e.*, relatively high IP(**A**) and EA(**B**), were imposed for RedQs. For specific applications, quantitative thresholds on IP(**A**) and EA(**B**) can be introduced to ensure that the GS and ES redox potentials are thermodynamically compatible with the full photocatalytic cycle. However, since the aim of this study is to propose a general screening protocol rather than to optimize the PC for a specific reaction, we have not imposed any specific criteria for IP(**A**) and EA(**B**).

To identify the best-performing systems, the systems were ranked with respect to four key descriptors, aimed at maximizing the charge-transfer (CT) characteristic while maintaining the optimal redox properties of **AB*** for the electron exchange with SUB/SA/SD:

(1) The gap between $E_{HOMO(A)}$ and $E_{HOMO(B)}$ (ΔHOMO) should be maximized;

(2) IP(**A**) should be minimized (OxQ)/maximized (RedQ);

(3) EA(**B**) should be minimized (OxQ)/maximized (RedQ);

(4) The difference between E_{HOMO}–E_{LUMO} gaps (ΔHL) should be maximized.

Based on this evaluation, 15 best candidates per quenching type were selected for further analysis, which was focused on examining the aggregation properties. First, the preferences for forming **AA**, **BB**, and **AB** stacks were addressed to identify PAH pairs favoring the **AB** arrangement. To this end, the lowest energy conformers of each type were found and their complexation energies were computed (see Computational details). Then, the feasibility of the aggregation in proper stacking arrangement resulting in e^-/h^+ located on the surface of OxQ*/RedQ* was assessed by exploring the stability of PAH tetramers. In particular, the systems preferring the **BAAB** and **ABBA** arrangements for the oxidative and reductive quenching pathways, respectively, were sought after. Finally, full quantum chemical analysis of electronic transitions and redox potentials of the best OxQ and RedQ systems was performed.

Input dataset of PAHs and computational details

Input dataset of the monomer systems contained various derivatives of (nitrogen-doped) anthracene, pyrene, and perylene (Fig. 2). Several electron-donating groups (–CH_3, –OMe, –NH_2, and –$N(Me)_2$) and electron-withdrawing substituents (–CN, –CHO, –F, and –COOMe) were considered. We note that the fluoro-substitution was considered due to the anticipated significant effects on the electronic structure of PAH

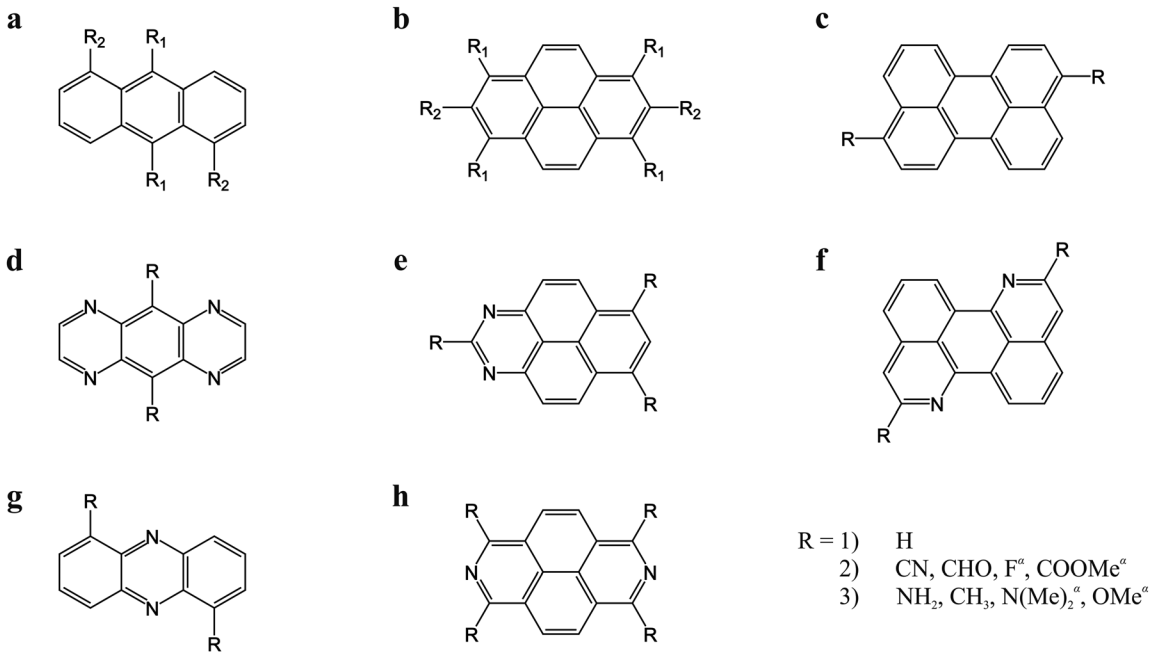

Fig. 2 Monomer systems of PAH investigated in this study. In cases where both R_1 and R_2 functional group positions are listed, only one of these options was utilized for one molecule. For all PAH cores, only one type of substituent was applied at the same time. Functional groups denoted with a superscript α were investigated for both undoped and N-doped pyrene cores.

derivatives, but the potential for their practical application would be limited by expected increased toxicity and low biodegradability of fluorinated compounds. The doping sites and substituent positions were selected based on the experimental availability of analogous systems and potential follow-up experimental studies.[47–55] Overall, the selected set of monomers was intended to provide a representative and chemically meaningful subset of the broader PAH chemical space, balancing structural diversity, synthetic feasibility, and coverage of key electronic features (*e.g.*, IP, EA, and orbital alignment) relevant to photocatalytic applications. This is further supported by the broad and continuous distribution of key descriptors (ΔHOMO, IP, EA, ΔHL), demonstrating the dataset's tunability and relevance for CT-based photocatalysis. All investigated structures were optimized at the ωB97XD/def2-SVP/*vacuum* level of theory. The monomer properties used as descriptors in further analyses were calculated at the same level and included E_{HOMO}, E_{LUMO}, IP and EA, with the latter two evaluated in the adiabatic regime. The calculations were carried out using the Gaussian16 program.[56]

The complexation energies of PAH dimers and tetramers were computed at the DFTB3-D3 level with the ob3 parameter set[57,58] using the DFTB+ program.[59] To identify the lowest energy conformer for each dimer, the centers of mass of monomers were set at a starting *Z*-axis distance of 3.2 Å and scanned at the 45° mutual rotation grid. Starting from these grid points, the systems were optimized, and the lowest energy conformer was used for further evaluation. For the optimization of tetramers, the starting structures were generated using the grid point settings, which resulted in the lowest energy **AA**, **AB** and **BB** complexes. Given the expected dominance of dispersion–interaction components, we also analyzed the correlation between the complexation energies and the respective molecular volumes of subsystems represented by the cavity volume values obtained using IEF–PCM calculations with default settings in Gaussian16. To complement the static calculations and explore the formation of larger aggregates, molecular dynamics (MD) simulations were performed at 300 K using GROMACS (version 5.1.2)[60] with the OPLS-AA[61] force field and an explicit dichloromethane (DCM) solvent model (see section S5 in the SI for more details). This solvent was selected as it was used for absorbance and emission spectra measurements of similar systems.[47,50,62]

Unless stated otherwise, electronic singlet transitions of studied systems were analyzed using TD-DFT with the ωB97XD functional and the def2-SVP/def2-TZVP basis sets as implemented in Gaussian16. The excited-state computations applying the simplified time-dependent (sTD)[63,64] approach and simplified Tamm-Dancoff approximation (sTDA) in combination with the ωB97X-D3 functional were performed with the ORCA 5.0.3 program.[65,66] Using the same program suite, the spin–orbit coupling terms were evaluated within Tamm-Dancoff approximation (TDA) at the ωB97X-D3/def2-TZVP/*vacuum* level with the scalar relativistic ZORA Hamiltonian. Whenever applied, the solvent effects of DCM on electronic transitions and geometry were taken into account by using the universal solvation model based on the solute electron density (SMD)[67] with the solvent excluding surface cavity. While the SMD model captures bulk solvation effects, it does not account for specific interactions or dynamic environmental factors such as solvent reorganization, which may influence the energetics and mechanism of intermolecular charge transfer. Nevertheless, as a continuum approach, it provides a consistent approximation of time- and ensemble-averaged solvation effects, appropriate for evaluating ground- and excited-state properties within the present framework, which focuses on comparisons among a diverse set of molecular assemblies built from similar building blocks.

For the decomposition of electronic transitions into LE and CT contributions, fragment-based analysis of correlated electron–hole pairs was used as defined by Plasser *et al.*[68–70] and implemented in the Theodore package.[71] In this analysis, omega matrices (Ω) for selected fragments and electronic transition are defined as follows:

$$\Omega_{\mathbf{AB}}^{0\mathrm{I}} = \sum_{\alpha\in\mathbf{A}}\sum_{\beta\in\mathbf{B}} \left(S^{1/2}D^{0\mathrm{I}}S^{1/2}\right)_{\alpha\beta}{}^2$$

relying on the Lowdin population analysis, with one-electron transition (D) and overlap (S) matrices evaluated in the atomic-orbital basis set and α and β labeling individual atomic orbitals. The molecular fragments were defined as **A** and **B** molecules in case of dimers, or alternatively as surface and core molecules that constituted the investigated **BAAB** and **ABBA** tetramer structures of OxQ and RedQ systems, respectively. The amount of the net charge that shifted from the fragment **A** to **B** $\left(\Delta_{q_{\mathbf{AB}}}^{0\mathrm{I}}\right)$ is then defined as follows:

$$\Delta_{q_{\mathbf{AB}}}^{0\mathrm{I}} = \left(\Omega_{\mathbf{AB}}^{0\mathrm{I}} - \Omega_{\mathbf{BA}}^{0\mathrm{I}}\right)/\Omega^{0\mathrm{I}}$$

with the sum $\Omega^{0\mathrm{I}} = \sum_{\mathbf{A},\mathbf{B}} \Omega_{\mathbf{AB}}^{0\mathrm{I}}$ close to 1 for the excited-state function defined as single-electron transition. The character of the transition is reflected in the individual $\Omega^{0\mathrm{I}}$ components, which distinguish between LE ($\Omega_{\mathbf{AA}}^{0\mathrm{I}}$, $\Omega_{\mathbf{BB}}^{0\mathrm{I}}$) and CT ($\Omega_{\mathbf{AB}}^{0\mathrm{I}}$, $\Omega_{\mathbf{BA}}^{0\mathrm{I}}$) contributions. These data were supplemented by charge-transfer diagnostics[72,73] that evaluates the measure of CT excitation length (D_{CT}) and the amount of transferred charge (q_{CT}) based on the variation in GS and ES electron densities.

The redox strengths of selected systems in their GS were calculated using a well-established protocol for the prediction of redox potentials of organic compounds.[74–78] The employed ωB97XD functional was shown to perform reasonably well for the redox properties of extended PAHs[79] as well as zirconocene organo-metal complexes.[78] For the redox potential in ES, a protocol based on a simplified Jablonski diagram proposed by Adamo and Jacquemin was utilized.[77,80] The absolute redox potential value of the saturated calomel electrode, $E°$(SCE) = 4.522 V,[81,82] was used as a reference throughout this work. Further details of the applied procedure are described in the SI (section S2).

3. Results and discussion

Selection of PAH pairs

The determined monomer properties (Table S1) formed a database for the selection of PAH pairs, fulfilling the posed criteria for mutual arrangement of the frontier orbital energies and IP and EA values of subsystems (the computed values for the best pairs are listed in Tables S2 and S24 in the SI). In total, 298 and 276 PAH pairs complied with the given requirements for oxidative and reductive quenching mechanisms, respectively. In the case of OxQ, the four monitored descriptors (ΔHOMO, IP(**A**), EA(**B**) and ΔHL) spanned the ranges (in eV) of (0.56, 2.96), (5.21, 6.74), (0.06, 1.39) and (0.35, 1.72), respectively. For the RedQ systems, the respective values spanned the intervals (0.54, 2.49), (6.78, 9.31), (1.52, 3.04) and (0.35, 1.07). The relatively large spans of values indicate high potential for the tunability of both optical and redox properties of PAH aggregates as PC species.

Subsequently, the filtered libraries were subject to further screening. Within the proposed strategy (Scheme 1), we utilized a system ranking with respect to the pre-set descriptors. To reiterate, the ranking should identify systems featuring strong CT characteristics of the lowest ES, good addressability of LE, high redox strength of the photoexcited aggregate and sufficient half-life of the ^{1}CT state. Accordingly, individual dimers were ordered to reduce the library to the highest-ranked 15 systems (listed in Fig. S2 and S17). The performance of individual dimers within the reduced sets is visualized using the heatmap representation (Fig. 3; the performance of the whole sets is shown in Fig. S3 and S18). For deeper characterization and discussion of the subsets, we now focus on OxQ and RedQ systems, in turn.

Selection of OxQ systems

Among the 15 best performing OxQ systems, three amino derivatives repeatedly occurred as **A** molecules, namely, 1,3,6,8-tetraaminopyrene, 1,3,6,8-tetra(dimethylamino)-2,7-diazapyrene, and 1,3,6,8-tetraamino-2,7-diazapyrene, displaying low IP(**A**) values (5.21, 5.33, and 5.38 eV, respectively) featured as donors within the subset. This was in line with the number of studies, which argued for the amination of (N-doped) PAH cores as a means to increase the reductive potential of the system.[83–85] Paired with these donors were various acceptor **B** molecules. The most prominent were either N-doped pyrene molecules or non-doped PAH cores (predominantly pyrene) with –F or –OMe substituents, but systems with other functional groups (–CH_3 and –COOMe) were also identified within the subset. As expected, electron-withdrawing groups in general increased EA values compared to their respective unsubstituted PAHs (Table S1). However, fluorinated derivatives featured an irregular trend. While the EA of 2,7-fluoropyrene (0.68 eV) was larger than that of pyrene (0.27 eV), 1,3,6,8-tetrafluoropyrene showed reverse behavior (0.09 eV) despite the LUMO energy decrease (0.22 eV with respect to pyrene). This observation can be explained by the ambiguous nature of the fluorine substituent, which displays negative inductive (–I) and positive mesomeric (+M) effects. In the case of the tetra-substituted derivative, this results in a reordering of frontier

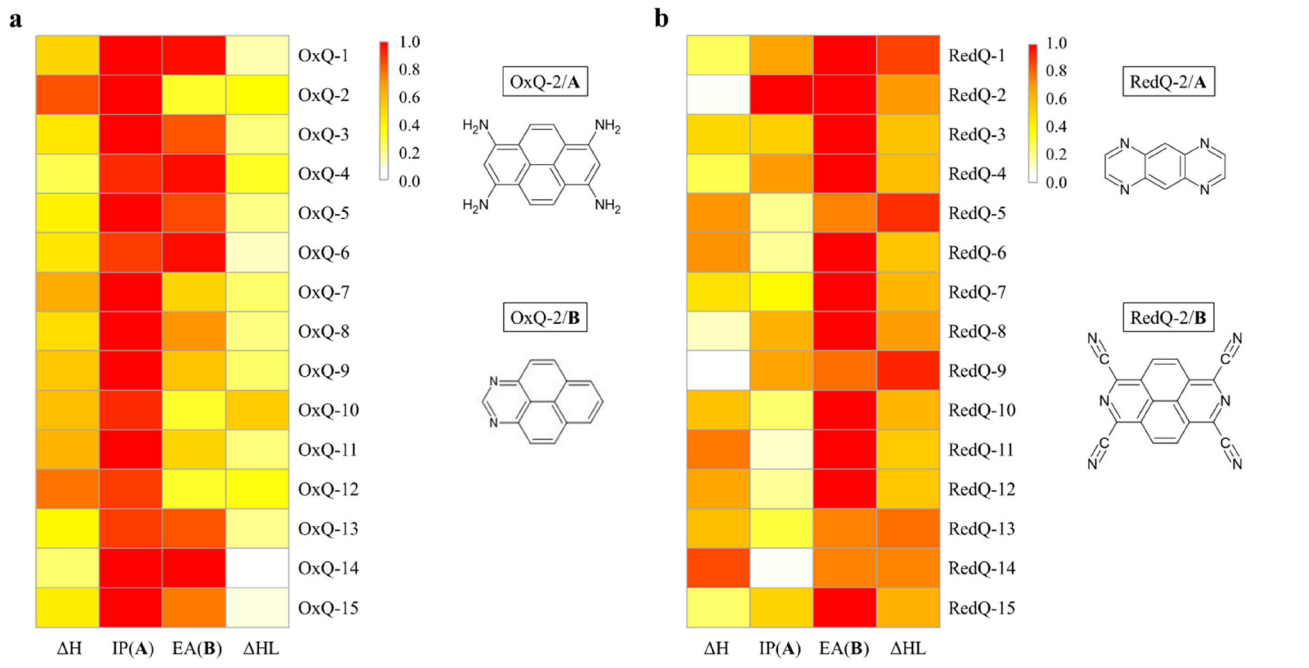

Fig. 3 Descriptor-performance heatmaps of the ordered (a) OxQ and (b) RedQ systems and the respective monomer molecules constituting the OxQ-2 and RedQ-2 dimers selected for deeper analysis. Color representation was set to vary from red (1.0, optimal) to white (0.0, suboptimal) descriptor values scaled according to eqn (S1). The scaling reflected the performance of systems according to the descriptors for the whole respective libraries (see full evaluation in the SI; Fig. S3 and S18). The notation OxQ-*X*/*Y* is used with *X* representing the number position of the dimer and *Y* notes whether the molecule is considered as **A** or **B** constituent of the agglomerate.

MOs after accepting an electron. The extra electron enters a MO more localized in the molecular core, which is electron depleted due to the –I effect of fluorines (see the electrostatic potential map in Fig. S1), whereas in pyrene, it occupies a different MO, which enables better delocalization of the negative charge, and thus leads to higher EA.

The analysis of monomer descriptors was further supplemented by information about the stacking preferences in terms of dimer interaction energies (Table S3). Assuming equal amounts of the constituents, the formation of two **AB** complexes should be more favorable than (or comparable to) the formation of **AA** and **BB** dimers. Furthermore, in the case of extended stacking of OxQ systems, the monomers need to prefer assemblies with the potential to create a reductive site on the surface after excitation. For tetramer structures, this translates into the requirement for the interaction energy of **AA** to be the highest out of the three possibilities to ensure the preference for forming **BAAB** stacks. From the subset of the 15 systems, only four pairs meet both listed criteria. From the perspective of molecular constituents, 1,3,6,8-tetraaminopyrene (OxQ-1 and OxQ-2) and 1,3,6,8-tetraamino-2,7-diazapyrene (OxQ-6 and OxQ-12) function as donor **A** molecules. Both molecules are combined with either 1,3,6,8-tetrafluoropyrene (OxQ-1,6) or 1,3-diazapyrene (OxQ-2,12) as acceptor **B** molecules. For deeper analysis and characterization in the following section, we will focus on the second system termed OxQ-2 (Fig. 3a), skipping OxQ-1 featuring extensive fluorine content that would limit its practical applicability.

Formation of a charge-transfer state in OxQ-2

Having selected the PAH pairs with the most promising characteristics for the oxidative quenching mechanism, we explored the nature and the ordering of their excited states, starting with the OxQ-2 system. Unless stated otherwise, the electronic transitions were analyzed at the ωB97XD/def2-TZVP/*vacuum* level using the DFTB/*vacuum* optimized geometries, which was found to be a reasonable protocol compared to more accurate approaches for the lowest excited state and bright transitions with $f > 0.1$ (see the SI for comparisons). The sTDA method also provided fair accuracy compared to TD-DFT. Although a state-switching was observed in several cases, it was limited to energetically higher singlet states.

The formation of the stacked dimer markedly affects the electronic transitions compared to its isolated constituents (Fig. 4 and Table S7). The most notable distinction is the emergence of an intermolecular CT state as the energetically lowest (2.37 eV) singlet excited state. The roles of **A** and **B** molecules as electron donors and acceptors, respectively, can be clearly distinguished from the electron density difference (EDD) plot (Fig. 4b) and the associated LE and CT components (Fig. 4c). Furthermore, the transition exhibits a low oscillator strength (0.06), suggesting its longer lifetime and thus increased chance for reactivity. The optimization of the GS geometry at the ωB97XD/def2-SVP/*vacuum* level introduces only a small (0.04 eV) redshift in $S_0 \rightarrow S_1$ transition energy and reduces its oscillator strength to 0.05. In DCM, the CT state is slightly stabilized (to 2.29 eV) and its oscillator strength increases to 0.11, as evaluated at the ωB97XD/def2-SVP/SMD(DCM) level, which significantly decreases the half-life of the state. The characteristic of $S_0 \rightarrow S_1$ however remains unchanged, with the dominant CT contribution preserved after solvation (Fig. S8b). For higher ESs, the EDD plots of $S_0 \rightarrow S_2$ and $S_0 \rightarrow S_3$ transitions closely resemble the two lowest transitions ($S_0 \rightarrow S_1$ and $S_0 \rightarrow S_2$, respectively) of the isolated **A** monomer. While

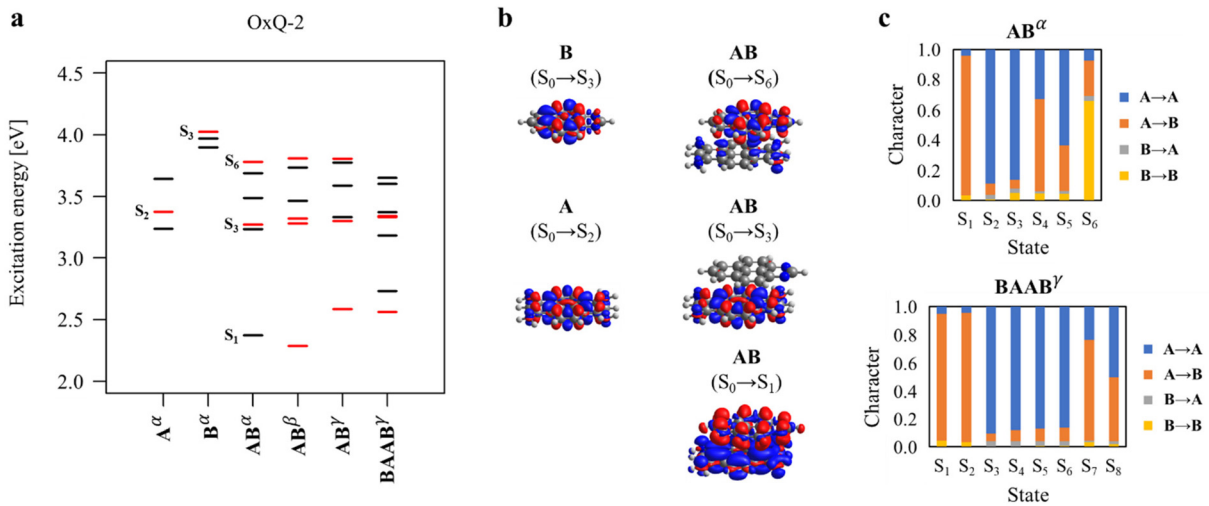

Fig. 4 (a) Singlet (S) excitation energies of OxQ-2 in form of its monomer constituents, **AB** dimer and **BAAB** tetramer, computed at the TD-ωB97XD/def2-TZVP/*vacuum* (*α*), TD-ωB97XD/def2-SVP/SMD(DCM) (*β*), and sTDA-ωB97X-D3/def2-TZVP/*vacuum* (*γ*) levels. For geometry optimization, DFTB/*vacuum* (*α*, *γ*) and ωB97XD/def2-SVP/SMD(DCM) (*β*) approaches were employed. Electronic transitions with computed an oscillator strength of >0.1 are shown in red. (b) EDD plots of the marked transitions with blue and red regions marking electron depletion and increase, respectively. EDD plots are based on ωB97XD/def2-SVP/*vacuum* densities. (c) Decomposition of individual singlet transitions into LE and CT components. For the tetramer, the contributions were scaled to obtain 1.0 after summation.

the former keeps the low oscillator strength and is energetically mostly unaffected, the latter is notably red-shifted (from 3.38 eV to 3.27 eV) and displays reduced but still significant oscillator strength (from 0.49 to 0.21). The $S_0 \rightarrow S_6$ transition is also bright ($f = 0.27$) and closely resembles the bright $S_0 \rightarrow S_3$ transition ($f = 0.28$) of the isolated **B** molecule, albeit it is red-shifted (from 4.03 eV to 3.78 eV).

The stability of the excited OxQ-2 system could be significantly increased, provided that ISC to a triplet state would be efficient. To explore the feasibility of such an event, we examined the singlet–triplet (S–T) energy splitting and the respective spin–orbit couplings (SOCs) in the optimized S_1 structure. In DCM, the geometry relaxation of the S_1 state results in significant stabilization of the lowest singlet transition, with a vertical de-excitation energy equal to 1.43 eV and $f = 0.00$. The TD-DFT calculations revealed T_1 and T_2 states as closest to the S_1 state, displaying −0.08 eV and 0.17 eV shifts, respectively. Despite the relatively small ΔE_{ST} between the S_1 and T_1, the spin–orbit coupling matrix element (SOCME) between those two states was found to be exceedingly small (0.02 cm^{-1}), and thus, the ISC event is unlikely for the OxQ-2 system.

Finally, the formation of CT states in larger aggregates was explored. As model systems, tetramers composed of two **A** and two **B** molecules, in which the surface and the core are already distinguishable while remaining computationally accessible for QM evaluation, were considered. The comparison of interaction energies of optimized clusters (Table S4) revealed the **BAAB** stack as preferential at the DFTB level. Subsequently, the electronic transitions were analyzed at the sTDA-ωB97X-D3/def2-TZVP/*vacuum* level, which performed well for the dimer (Table S7). In **BAAB**, the S_1 and S_2 states are of CT characteristics, with e^- and h^+ localized at the surface and the core, respectively (Fig. 4c). The oscillator of the S_1 state significantly increased upon aggregation to **BAAB** ($f = 0.15$) compared to the **AB** dimer ($f = 0.10$), which is an undesirable effect decreasing the half-life of the ^{1}CT state. Similar enhancement of the ^{1}CT oscillator strength due to the solvation and extended aggregation was also found for the other analyzed OxQ (Tables S13 and S15) and RedQ (Tables S29 and S31) systems. A higher bright transition ($S_0 \rightarrow S_5$) of OxQ-2/**BAAB** has an energy of 3.34 eV ($f = 0.16$) and dominant LE on the **AA** core (Fig. 4c). It resembles the LE transition on the molecule **A** of the **AB** dimer, with similar energy (3.30 eV) and oscillator strength (0.21).

Formation of a charge-transfer state in other OxQ systems

The increased brightness of the ^{1}CT state of OxQ-2 in DCM and after aggregation into the tetramer **BAAB** structure limits the usability of this system. Therefore, other OxQ systems were also analyzed before further characterization of associated redox properties. As mentioned, OxQ-1 was skipped due to fluorine substitution of the acceptor. Nonetheless, we offer the analysis of its electronic transitions in the SI (section S3.2).

Within the subset of the selected 15 OxQ systems, only OxQ-6 and OxQ-12 fulfilled the criteria on the dimer interaction energies. However, both systems have the same constituting **A** and **B** subunits as OxQ-1 and OxQ-2 (Fig. S2) with a slight difference in **A** molecule (2,7-N-doping of the pyrene core), and thus, presumably share the same issues. Indeed, OxQ-12 containing 1,3-diazapyrene (**B**) displays even a larger oscillator strength for the dimer ($f = 0.13$) than OxQ-2 ($f = 0.10$) (Table S7). We therefore extended the subset until a system fulfilled all discussed criteria, which was OxQ-32. While a higher positioned OxQ-29 also displayed a proper stacking behavior, a bright $S_0 \rightarrow S_1$ transition ($f = 0.10$) was evaluated at the sTDA-ωB97X-D3/def2-TZVP/*vacuum* level. OxQ-29 is composed of the same donor **A** molecule as OxQ-2, which is paired with 2,6,8-trimethyl-1,3-diazapyrene (**B**). The presence of the 1,3-diazapyrene core thus consistently resulted in an increased oscillator strength of the S_1 state of **AB** stacks. From the analysis of all investigated systems, including both OxQs and RedQs (*vide infra*), a connection of increased oscillator strength was related to the formation of slightly slipped **AB** stack structures and subsequent nonsymmetric partition of e^- and h^+ within the fragments and significant projected "drift" D_{CT} components (Tables S10, S16, S22 and S36).

The electronic transitions of OxQ-32, composed of 1,3,6,8-tetraaminopyrene (**A**) and 2,7-dicyanopyrene (**B**) (Fig. 5), are shown in Fig. 6 with detailed description provided in the SI (section S3.3). The S_1 state of the dimer has a clear CT character (Fig. 6c) and small oscillator strength ($f = 0.02$) (Table S19) in the vacuum. Although the DCM environment slightly increases the oscillator strength ($f = 0.05$) (Table S19), the value remains <0.1 and the transition can still be considered as dark. The major CT character of the S_1 state is also maintained upon the solvation (Fig. S16b). $S_0 \rightarrow S_4$ ($f = 0.16$) and $S_0 \rightarrow S_6$ ($f = 0.14$) represent LEs on **A** and **B** constituents, respectively, that are separated by about 0.19 eV. Analysis of the potential ISC upon relaxation to the S_1 state in DCM (Table S20) reveals a relatively small (0.06 eV) separation between the S_1 and energetically higher T_2 states. However, the SOCME for this pair is nil (0.00 cm^{-1}), which prevents the potential ISC event. The aggregation of OxQ-32 into energetically favorable **BAAB** assembly (Table S4) affects the electronic spectra only to a small degree (Fig. 6). Indeed, the $S_0 \rightarrow S_1$ transition keeps the dominant CT character and negligible oscillator strength ($f = 0.01$) and is only marginally (0.05 eV)

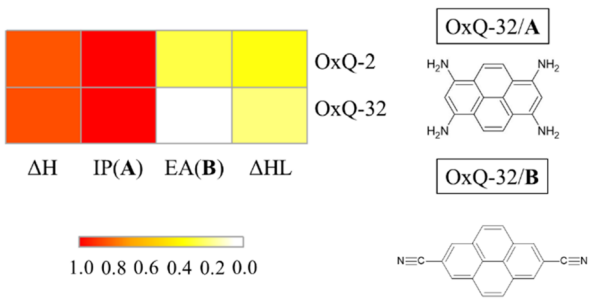

Fig. 5 Descriptor-performance heatmap of OxQ-2 and OxQ-32, SI to Fig. 3. The scaling reflected the performance of descriptors for the whole OxQ library (see full evaluation in the SI; Fig. S3).

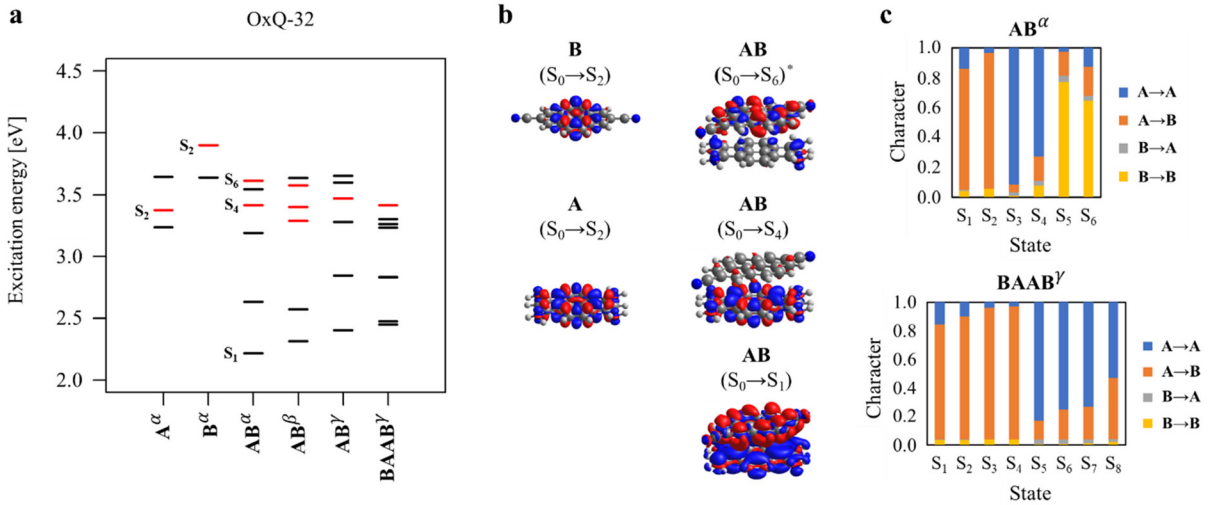

Fig. 6 (a) Singlet (S) excitation energies of OxQ-32 in form of its monomer constituents, AB dimer and BAAB tetramer, computed at the TD-ωB97XD/def2-TZVP/*vacuum* (α), TD-ωB97XD/def2-SVP/SMD(DCM) (β) and sTDA-ωB97X-D3/def2-TZVP/*vacuum* (γ) levels. For geometry optimization, DFTB/*vacuum* (α, γ) and ωB97XD/def2-SVP/SMD(DCM) (β) approaches were employed. Electronic transitions with a computed oscillator strength of >0.1 are shown in red. (b) EDD plots of the marked transitions with blue and red regions marking electron depletion and increase, respectively. EDD plots were based on ωB97XD/def2-SVP/*vacuum* densities. The AB($S_0 \rightarrow S_6$)* plot is represented by $S_0 \rightarrow S_7$ transition, given the state switching due to differences in used basis set (Table S19). (c) Decomposition of individual singlet transitions into LE and CT components. For the tetramer, the contributions were scaled to obtain 1.0 after summation.

red-shifted compared to the dimer at the sTDA-ωB97X-D3/def2-TZVP/*vacuum* level. The energetically lowest bright $S_0 \rightarrow S_8$ transition (f = 0.14) is shown to be of mixed CT(core → surface) and LE(core → core) characteristics, with a slightly larger contribution from the latter. MD simulations at 300 K confirmed the presence of long-lived **AB** aggregates in OxQ-32. However, the formation of extended **BAA**...-type architecture was hampered by the disordered aggregation of the A molecules (see section S5 in the SI). Nonetheless, OxQ-32 exhibits superior performance to OxQ-2 as similar aggregation behavior is expected due to the presence of the same A component.

Redox potentials of OxQ systems

To make the oxidative quenching mechanism operate, the formation of a charge-separated excited state needs to be supplemented by thermodynamic readiness of the electron-transfer processes between PC and SA/SUB. The latter can be described by means of redox potentials of the systems involved (Fig. 7). As an example of an electron acceptor SUB, we considered anthraquinone (AQ) with a computed value of $E°$(AQ/AQ$^-$) = −1.49 V in DCM. In the GS, all of the previously discussed OxQ systems have similar $E°$(OxQ$^+$/OxQ), with −0.72 V, −0.69 V and −0.64 V computed for OxQ-1, OxQ-2 and OxQ-32, respectively, as **AB** dimers in DCM. Clearly, each of these display too high redox potentials to reduce the AQ prior to excitation. The small spread of the values can be related to the presence of the same donor **A** molecule.

The electronic excitation of the complexes to their respective S_1 states, including geometry relaxation, introduced a significant negative shift of redox potentials. The most negative $E°$(OxQ$^+$/OxQ*) value was computed for OxQ-1, with the redox potential reaching −3.04 V. For OxQ-2 and OxQ-32, close values of −2.54 V and −2.53 V were computed, respectively. Therefore, each of the excited OxQ* systems can be expected to readily reduce AQ. While the lowering of OxQ redox potentials upon excitation can be largely attributed to the $S_1 \rightarrow S_0$ de-excitation energy (1.94 eV, 1.38 eV, and 1.51 eV for OxQ-1, OxQ-2 and OxQ-32, respectively), the reorganization energy also plays an important role (0.38 eV, 0.48 eV, and 0.38 eV). From a perspective of monomer constituents, it is evident that the largest shift of $E°$(OxQ$^+$/OxQ) redox potential upon excitation of the dimer was computed for OxQ-1 with the smallest EA(**B**). Similar lowering of the ES redox potential relative to the GS was predicted for OxQ-2 and OxQ-32 with comparable EA(**B**) values.

Tuning of OxQ redox potentials

To design versatile reaction-specific CD-based photocatalytic systems, it is desirable to evaluate the possibility of tuning the redox potentials of designed PAH-based aggregates. Depending on the selection of SD, the ground-state $E°$(OxQ$^+$/OxQ) may be required to be shifted to more positive values, to enable the regeneration of the PC. However, harder to reduce SUBs may impose criteria on further decrease of $E°$(OxQ$^+$/OxQ*) of the photo-excited PC. For screening purposes, it is important to identify the monomer characteristics that are most relevant for the redox properties of the complex.

The GS $E°$(OxQ$^+$/OxQ) can be related to the adiabatic IP(**A**) value under the assumption that the dominant portion of generated h$^+$ is localized on the subsystem **A**. Therefore, the IP(**A**) value in DCM solvent, which was obtained by a single-point SMD calculation using the gas phase geometry and was shifted

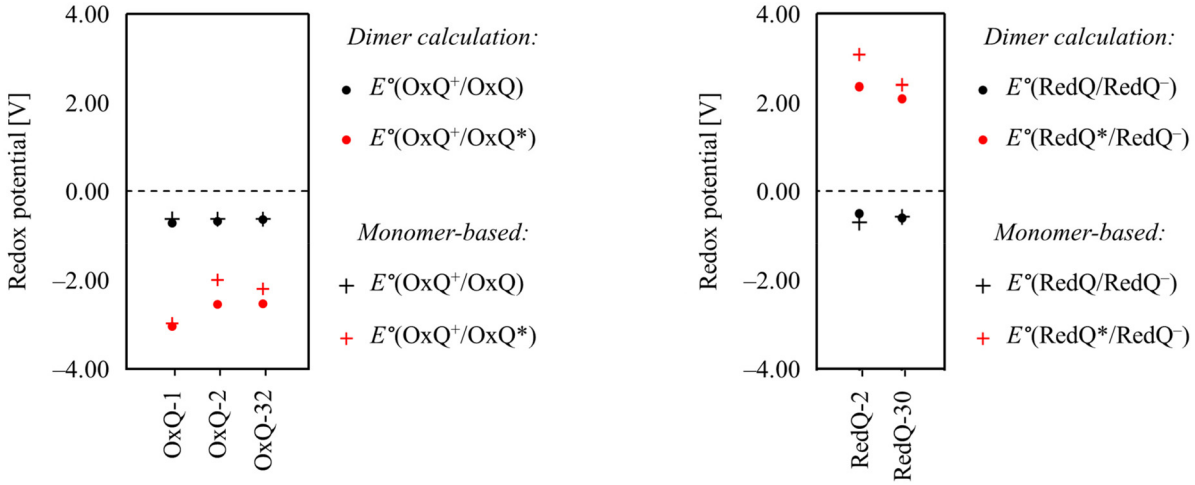

Fig. 7 Redox potentials of the investigated OxQ and RedQ dimers in DCM in their GS (black) and ES (red). Both values computed for the dimers (dots) and those approximated based on monomer descriptors (crosses) are visualized. All computed values were evaluated given $E°$(SCE) = 4.522 V.

by E°(SCE), can serve as a basis for the E°(OxQ^+/OxQ) approximation. For the OxQ-1, OxQ-2 and OxQ-32 systems, the donor **A** constituent is the same (1,3,6,8-tetraaminopyrene) with the approximate $E°(OxQ^+/OxQ)$ = −0.62 V. This is in good agreement with −0.72 V, −0.69 V and −0.64 V computed for the OxQ-1, OxQ-2 and OxQ-32 dimers, respectively.

The ES $E°(OxQ^+/OxQ^*)$ can be related to EA(**B**) in DCM. Evidently from eqn (S5), the same descriptor is also obtained if $E°(OxQ^+/OxQ)$ is approximated by IP(**A**) and the shift due to the sum of vertical fluorescence energy and reorganization energy is considered to equal IP(**A**)–EA(**B**) in the adiabatic regime. The latter assumption becomes more appropriate as the CT(**A** → **B**) character of the S_1 state increases. Under these approximations, the values of −2.98 V, −1.99 V and −2.20 V were calculated for OxQ-1, OxQ-2 and OxQ-32, respectively, which were in fair agreement with the dimer values of −3.04 V, −2.54 V and −2.53 V. Despite the evident trend of increased agreement with the enhanced IP(**A**)–EA(**B**) difference, this observation is not directly related to the amount of intermolecular CT(**A** → **B**) contribution to $S_1 \rightarrow S_0$ deexcitation. Indeed, the analysis of this transition in DCM shows $\Delta^{0S_1}q_{\mathbf{AB}}$ values of 0.94, 0.95 and 0.88 evaluated from Ω matrices and q_{CT} values of 1.20, 1.21 and 1.12 for OxQ-1, OxQ-2 and OxQ-32, respectively. Clearly, other factors like mutual spatial positioning of interacting monomers significantly affect the properties of the systems, and more complex interplay of descriptors would need to be considered for the accurate prediction of ES redox potential for OxQ systems in general.

Selection of RedQ systems

RedQ systems can be explored in the same spirit as those proposed for the oxidative quenching pathway. Here we will focus on the main points, with more detailed discussion available in the SI. Fig. 3 shows a heatmap of 15 best performing RedQ systems according to the set descriptors. Interestingly, a comparison of the highly ranked OxQs and RedQs revealed that about half of the acceptor **B** monomers of the former were also present as donor **A** moieties in the latter group. Namely, unsubstituted pyrene, 1,3-diazapyrene, 2,7-diazapyrene and 2,7-disubstituted pyrenes with methyl, fluorine, methoxy and methoxycarbonyl groups were included in both subsets, acting as reactive centers in the ^{1}CT state of PAH pairs. A RedQ-2 complex containing pyrazino[2,3-*g*]quinoxaline and 1,3,6,8-tetracyano-2,7-diazapyrene as **A** and **B** subsystems, respectively, was selected for further analyses, as RedQ-1 did not satisfy the stacking preference criteria (Table S25).

Formation of a CT state in RedQ systems

Analysis of the electronic transitions of RedQ-2 confirmed the lowest transition (2.96 eV) as an intermolecular CT state (Fig. S19) with dominant HOMO → LUMO character and nil oscillator strength (0.00) in the vacuum (Table S29). While the DCM solvent did not significantly affect the $S_0 \rightarrow S_1$ transition energy, the oscillator strength increased dramatically to a value of 0.37. This was related to a considerable decrease of $E_{HOMO(A)}$–$E_{HOMO(B)}$ (from 0.68 eV to 0.10 eV) after transferring from the vacuum to DCM, which caused a notable reduction in the CT character of the $S_0 \rightarrow S_1$ transition in favor of a more pronounced LE component, which was also evident from EDD plots (Fig. S22 and S23) and state-decomposition plots (Fig. S25). This contrasted with the investigated OxQ systems discussed above for which ΔHOMO after solvation remained large (>1.5 eV). An increase in the oscillator strength and dominancy of the LE character of the S_1 state of the RedQ-2 dimer was also observed for **ABBA** tetramers (Fig. S19c), showing that not only solvation, but also extended aggregation is detrimental for achieving a long-living charge-separated state of RedQ-2.

These observations significantly diminish the applicability of the RedQ-2 system. Within the subset of the 15 RedQ systems, only RedQ-4, RedQ-8 and RedQ-9 fulfilled the dimer interaction criteria. However, the ΔHOMO values were again

very low in DCM (0.43, 0.40 and 0.19 eV, respectively). This also reflected poorly on the oscillator strengths of their $S_0 \rightarrow S_1$ transitions with f = 0.40, 0.26 and 0.47, respectively (Table S25). We have therefore extended the computation of the dimer interaction energies, skipping molecules with a fluorine substituent, until another system fulfilling the criteria was identified. The first confirmed system was RedQ-30, with 1,3-diazapyrene and pyrazino[2,3-*g*]quinoxaline-5,10-dicarbonitrile as **A** and **B** molecules, respectively (Fig. 8). The ΔHOMO value was sufficiently high (0.94 eV in DCM), and the system displayed S_1 state with nil oscillator strength (0.00) (Table S33). We note that despite the evident connection of low ΔHOMO values to the high oscillator strength of the dimer presented here, this parameter is not the sole descriptor that ensures the vanishing f of the ^{1}CT state. Indeed, as discussed in the previous section, the OxQ-2 system also displayed slightly bright transition in DCM (f = 0.11) despite the pronounced ΔHOMO value (2.32 eV). Remarkably, while the slightly higher f of ^{1}CT transition in OxQ-2 was attributed to the formation of a slipped **AB** stack (Table S10), this effect was not present in RedQ-30 despite the similar – albeit less – drifted conformation adopted by its **AB** dimer (Table S36). Ciofini's charge-transfer diagnostic DCT (Tables S10 and S36) and Ω matrix-based state decompositions (Tables S11 and S37) of the respective ^{1}CT states showed that the crucial difference lied in the greater asymmetry of h^+ and e^- partition in the case of OxQ-2. However, a larger dataset would be needed to find out whether some qualitative criteria on the maximum mutual special drift (or other parameters) can be imposed to ensure vanishing f for similar systems during the system screening.

The lowest electronic transitions of the RedQ-30 dimer and its monomer constituents are shown in Fig. 9, with a detailed overview presented in the SI (section S4.2). From the EDD plots (Fig. 9b) and associated LE and CT contributions (Fig. 9c) it is evident that the S_1 state has dominant CT(**A** → **B**) character. The energetically lowest bright transition ($S_0 \rightarrow S_4$) has a distinct LE(**B** → **B**) nature, with comparable energy to $S_0 \rightarrow S_3$ transition of the isolated **B** molecule, but with slightly reduced oscillator strength. The bright state with dominant LE (**A** → **A**) was not observed for the **AB** dimer, as expected from the high energy (>4 eV) of the bright state of the isolated **A** molecule (Table S6). Analysis of the triplet states of the RedQ-30 dimer in its S_1 geometry in DCM (Table S34) revealed a moderate energy gap between S_1 (2.27 eV) and energetically lower T_2 (2.00 eV) states, whereas T_3 (2.45 eV) was slightly closer in terms of energy. The evaluated SOCME between the S_1 and T_3 states (ΔE_{ST} = 0.18 eV) was largest across all investigated systems (0.25 cm^{-1}), yet remains small and thus the ISC event is unlikely. The improbability of ISC is thus a consistent finding across all systems that were characterized in this study.

The effects of extended aggregation on electronic transitions were also investigated at the tetramer level. It is clear from the analysis (Table S35) that the **ABBA** stacking order is the most preferred with defined surface-donor and core-acceptor regions. The aggregation only marginally (0.04 eV) stabilizes the energy on the S_1 state, and the transition keeps nil oscillator strength (f = 0.00) and has dominant CT(surface → core) contribution. However, the energy of the energetically lowest bright transition is largely blue-shifted to 3.60 eV when compared to the dimer (3.36 eV) and has a mixed LE(core → core) and CT(surface → core) character (Fig. 9). Despite this, the **ABBA** aggregate keeps the potential for selective excitation to the S_9 state, with the next bright transition ($S_0 \rightarrow S_{19}$; f = 0.17) substantially distanced at 4.11 eV. These findings were further supported by room-temperature MD simulations, which confirmed the formation of stable **AB** aggregates and the emergence of larger **ABB…**-type architecture featuring exposed **A** molecules (see section S5 in the SI).

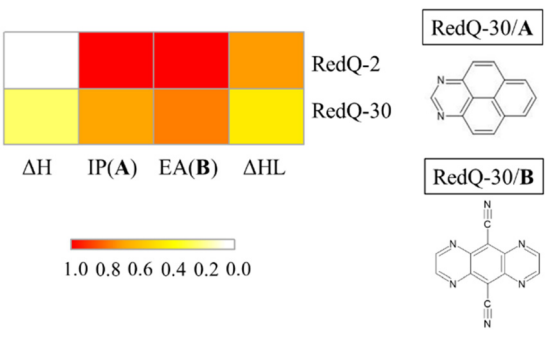

Fig. 8 Descriptor-performance heatmap of RedQ-2 and RedQ-30, supplementary to Fig. 3. The scaling reflected the performance of descriptors for the whole RedQ library (see full evaluation in the SI; Fig. S18).

Redox potentials of RedQ-30

Evaluated redox potentials of RedQ-30 are shown in Fig. 7. For the solvated dimer in the GS, the $E°$(RedQ-30/RedQ-30$^-$) of −0.61 V was obtained. Upon excitation and relaxation to the S_1 state, the redox potential is increased significantly to $E°$(RedQ-30*/RedQ-30$^-$) = 2.08 V. Based on these redox potentials, the photo-excited RedQ-30(**AB**)* should display more than sufficient thermodynamic characteristics for the oxidation of commonly used SD triethanolamine (TEOA) with the evaluated redox potential of $E°$($TEOA^+$/TEOA) = 0.73 V.

Based on monomer descriptors, IP(**A**) and EA(**B**), the redox potentials for RedQ systems can be approximated to allow for potential screening. The GS $E°$(RedQ-30/RedQ-30$^-$) value is related to EA(**B**) under the assumption that the received e^- becomes localized solely on the **B** constituent and its stability is not significantly affected by intermolecular interactions within the stack. In DCM, this leads to an estimate of −0.58 V for RedQ-30, which is in excellent agreement with the values evaluated for dimer (−0.61 V). For the excited complex, the insolvent IP(**A**) value represents the thermodynamic readiness for e^- to be accepted by the photoexcited system. Given this, the monomer-based $E°$(RedQ-30*/RedQ-30$^-$) of 2.39 V was evaluated, which is in good agreement with the quantity computed for the dimer by DFT calculations (2.08 V).

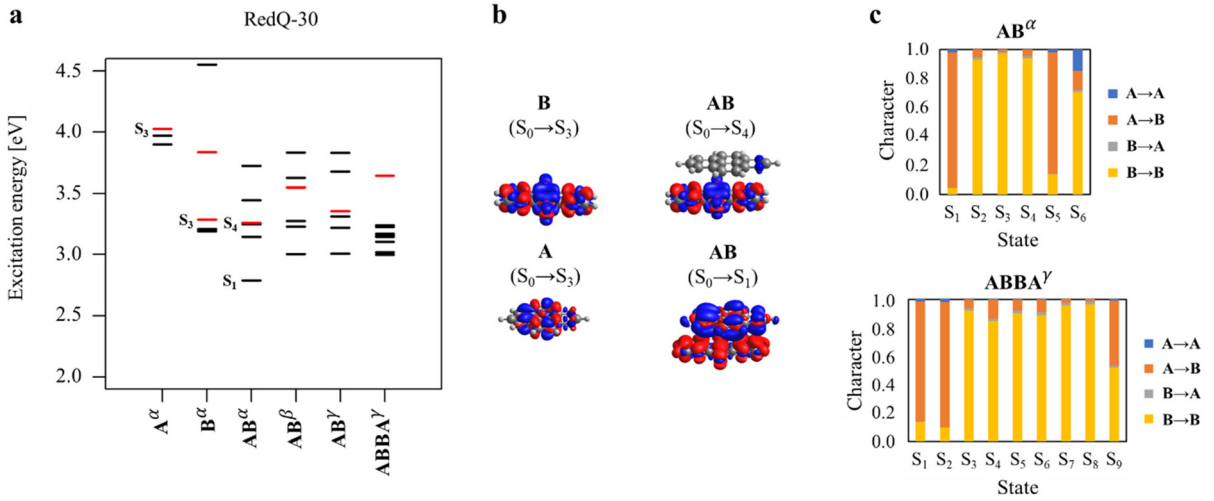

Fig. 9 (a) Singlet (S) excitation energies of RedQ-30 in the form of its monomer constituents, AB dimer and BAAB tetramer, computed at the TD-ωB97XD/def2-TZVP/*vacuum* (α), TD-ωB97XD/def2-SVP/SMD(DCM) (β) and sTDA-ωB97X-D3/def2-TZVP/*vacuum* (γ) levels. For geometry optimization, DFTB/*vacuum* (α, β) and ωB97XD/def2-SVP/SMD(DCM) (b) approaches were employed. Electronic transitions with a computed oscillator strength of >0.1 are shown in red. (b) EDD plots of the marked transitions with blue and red regions marking electron depletion and increase, respectively. EDD plots were based on ωB97XD/def2-SVP/*vacuum* densities. (c) Decomposition of individual singlet transitions into LE and CT components. For the tetramer, the contributions were scaled to obtain 1.0 after summation.

4. Conclusions

We proposed a computational protocol for the identification of stacked PAH complexes possessing essential characteristics for photoredox catalytic applications such as the CT character of the S_1 state, addressable bright local excitations, convenient redox properties, and readiness for aggregation preserving the core-surface charge separation in the lowest excited state. The well-defined structures allow for the elucidation of fundamental photophysical processes occurring in the otherwise highly complex CD architecture by using both advanced theoretical approaches and modern time-resolved spectroscopies. While real CDs often exhibit significant heterogeneity, the π-stacked PAH complexes and aggregates explored here represent model systems that capture key structural and electronic motifs found in CD-like materials. As such, the protocol offers a bottom-up design framework for constructing donor–acceptor architecture with high structural interpretability—a feature that can aid in correlating molecular-level properties with experimental CD behavior. Pertinent molecular descriptors, such as IP, EA, and frontier orbital energies, have been used to filter and rank a library of PAH derivatives with nitrogen doping sites and functionalization positions selected based on the experimental availability of analogous systems. The dataset of 5700 D–A pairs was split to account for alternate oxidative and reductive quenching mechanisms, with 15 highest ranked OxQ and RedQ systems initially considered for further DFT analysis. Among the OxQ systems, NH_2 functionalization was predominantly observed in best-performing electron donors, whereas the RedQ systems frequently showed the presence of CN groups on the electron acceptors. In contrast, the complementary acceptors (in OxQ) and donors (in RedQ) exhibited greater chemical diversity, spanning a wider range of sp^2 domain sizes, nitrogen doping patterns, and substitution motifs. This diversity highlights the high potential for tuning the electronic and structural properties of the resulting donor–acceptor complexes. To further refine the candidate selection, dimer interaction energies were evaluated to identify systems with stacking preferences that ensure favourable D–A paring, coupled with the resolved core-surface tetramer arrangement. Fulfilling all imposed criteria, the highest ranked OxQ-2 (1,3,6,8-tetraaminopyrene/1,3-diazapyrene) and RedQ-2 (pyrazino[2,3-*g*]quinoxaline/1,3,6,8-tetracyano-2,7-diazapyrene) systems were initially characterized in the vacuum, and showed promising photo-physical properties. However, the introduction of the DCM solvent environment and extended aggregation resulted in worsened performance of both systems due to significantly increased oscillator strength (to >0.1) of respective S_1 states. In the case of OxQ-2, this was associated with the tendency to form slightly slipped **AB** stacks with uneven partition of h^+ and e^- within the **A** and **B** fragments, whereas RedQ-2 displayed a loss of CT character of the S_1 state connected to a decrease in the ΔHOMO descriptor in DCM. These observations underscore the importance of control of both structural and electronic features, particularly π–π stacking geometry and the frontier MO gap thresholds, for achieving desirable characteristics of critical ESs. With these in mind, the OxQ-32 (1,3,6,8-tetraaminopyrene/2,7-dicyanopyrene) and RedQ-30 (1,3-diazapyrene/pyrazino[2,3-*g*]quinoxaline-5,10-dicarbonitrile) systems were identified as suitable alternatives exhibiting improved performance with dark charge-separated S_1 states that persisted in the solvent as well as upon aggregation to the tetramer structure. In addition, the energetically lowest bright transitions remained in the near-UV region (3.4–3.6 eV). From a

thermodynamic standpoint, the photo-excited OxQ-32 and RedQ-30 complexes have shown significant reductive and oxidative power, respectively, and featured a modest redox potential shift due to the excitation (1.9–2.7 V). Within the procedure, monomer descriptors were able to screen the redox potentials of those systems with errors up to 0.03 V and 0.33 V for GS and ES, respectively. Overall, our results showed that the proposed protocol allows for the identification of PAH-based donor–acceptor complexes with predictable and tunable optical and redox properties.

Author contributions

M. O. and M. M. conceptualized the project. T. H. performed the *ab initio* calculations and was responsible for data curation. M. P. performed MD simulations. T. H. and M. M. wrote the original draft. The manuscript was reviewed and edited through contributions of all authors. M. O., M. M., and A. R. secured funding. All authors have given approval to the final version of the manuscript.

Conflicts of interest

There are no conflicts to declare.

Data availability

The data supporting the results of this study are openly available in the Zenodo repository at **https://doi.org/10.5281/zenodo.17129455**. Additional references have been cited within the SI.[86–94] Supplementary information associated with this article is available at **https://doi.org/10.1039/d5nr02170g**. (including details on design strategy, redox potential calculations, excitation energies, dimer and tetramer interaction energies, and molecular dynamics simulations).

Acknowledgements

This work was supported by the project "Experimental and theoretical studies of near-infrared-emitting and chiral carbon dot luminophores" from the Moravian-Silesian Region, contract no. 00734/2023/RRC, and by the ERDF/ESF project TECHSCALE (No. CZ.02.01.01/00/22_008/0004587). M. M. acknowledges the support of the Slovak Research and Development Agency (APVV-20-0098). The COST Action CA21101 is also acknowledged. T. H. acknowledges the funding from grants APVV-21-0346 and VEGA 2/0098/23. This work was also supported by the Ministry of Education, Youth and Sports of the Czech Republic through the e-INFRA CZ (ID: 90254). This article has also been produced with the financial support of the European Union under the REFRESH (Research Excellence For Region Sustainability and High-tech Industries) project number CZ.10.03.01/00/22_003/0000048 *via* the Operational Programme Just Transition.

References

1 K. Hola, Y. Zhang, Y. Wang, E. P. Giannelis, R. Zboril and A. L. Rogach, *Nano Today*, 2014, **9**, 590–603.
2 B. Wang, H. Cai, G. I. N. Waterhouse, X. Qu, B. Yang and S. Lu, *Small Sci.*, 2022, **2**, 2200012.
3 D. Ozyurt, M. Al Kobaisi, R. K. Hocking and B. Fox, *Carbon Trends*, 2023, **12**, 100276.
4 H. Liu, X. Zhong, Q. Pan, Y. Zhang, W. Deng, G. Zou, H. Hou and X. Ji, *Coord. Chem. Rev.*, 2024, **498**, 215468.
5 B. Wang and S. Lu, *Matter*, 2022, **5**, 110–149.
6 L. Ai, Y. Yang, B. Wang, J. Chang, Z. Tang, B. Yang and S. Lu, *Sci. Bull.*, 2021, **66**, 839–856.
7 B. Wang, J. Yu, L. Sui, S. Zhu, Z. Tang, B. Yang and S. Lu, *Adv. Sci.*, 2021, **8**, 2001453.
8 G. Ragazzon, A. Cadrane, E. V. Ushakova, Y. Wang, D. M. Guldi, A. L. Rogach, N. A. Kotov and M. Prato, *Chem*, 2021, **7**, 606–628.
9 L. Zdražil, A. Cadranel, M. Medveď, M. Otyepka, R. Zbořil and D. M. Guldi, *Chem*, 2024, **10**, 2700–2723.
10 L. Đorđević, F. Arcudi, M. Cacioppo and M. Prato, *Nat. Nanotechnol.*, 2022, **17**, 112–130.
11 S. Khan, A. Sharma, S. Ghoshal, S. Jain, M. K. Hazra and C. K. Nandi, *Chem. Sci.*, 2018, **9**, 175–180.
12 Y. Reva, B. Jana, D. Langford, M. Kinzelmann, Y. Bo, P. R. Schol, T. Scharl, X. Zhao, R. W. Crisp, T. Drewello, T. Clark, A. Cadranel and D. M. Guldi, *Small*, 2023, **19**, 2207238.
13 W. Liang, S. K. Sonkar, D. Saini, K. Sheriff, B. Singh, L. Yang, P. Wang and Y.-P. Sun, *Small*, 2023, **19**, 2206680.
14 Y. Xiong, J. Schneider, E. V. Ushakova and A. L. Rogach, *Nano Today*, 2018, **23**, 124–139.
15 M. Langer, L. Zdražil, M. Medveď and M. Otyepka, *Nanoscale*, 2023, **15**, 4022–4032.
16 L. Shi, J. H. Yang, H. B. Zeng, Y. M. Chen, S. C. Yang, C. Wu, H. Zeng, O. Yoshihito and Q. Zhang, *Nanoscale*, 2016, **8**, 14374–14378.
17 W. Kasprzyk, T. Świergosz, S. Bednarz, K. Walas, N. V. Bashmakova and D. Bogdał, *Nanoscale*, 2018, **10**, 13889–13894.
18 W. Kasprzyk, T. Świergosz, P. P. Romańczyk, J. Feldmann and J. K. Stolarczyk, *Nanoscale*, 2022, **14**, 14368–14384.
19 M. Langer, T. Hrivnák, M. Medved' and M. Otyepka, *J. Phys. Chem. C*, 2021, **125**, 12140–12148.
20 F. Siddique, M. Langer, M. Paloncýová, M. Medved', M. Otyepka, D. Nachtigallová, H. Lischka and A. J. A. Aquino, *J. Phys. Chem. C*, 2020, **124**, 14327–14337.
21 R. Bhuyan, B. Kommula, L. Bishwal, S. Mandal and S. Bhattacharyya, *J. Phys. Chem. C*, 2022, **126**, 16377–16386.
22 M. Shamsipur, A. Barati, A. A. Taherpour and M. Jamshidi, *J. Phys. Chem. Lett.*, 2018, **9**, 4189–4198.

23 F. Ehrat, S. Bhattacharyya, J. Schneider, A. Löf, R. Wyrwich, A. L. Rogach, J. K. Stolarczyk, A. S. Urban and J. Feldmann, *Nano Lett.*, 2017, **17**, 7710–7716.
24 C. Kang, S. Tao, F. Yang and B. Yang, *Aggregate*, 2022, **3**, e169.
25 F. Mocci, L. de V. Engelbrecht, C. Olla, A. Cappai, M. F. Casula, C. Melis, L. Stagi, A. Laaksonen and C. M. Carbonaro, *Chem. Rev.*, 2022, **122**, 13709–13799.
26 J. Yu, X. Yong, Z. Tang, B. Yang and S. Lu, *J. Phys. Chem. Lett.*, 2021, **12**, 7671–7687.
27 O. Kozák, M. Sudolská, G. Pramanik, P. Cígler, M. Otyepka and R. Zbořil, *Chem. Mater.*, 2016, **28**, 4085–4128.
28 S. Sarkar, M. Sudolská, M. Dubecký, C. J. Reckmeier, A. L. Rogach, R. Zbořil and M. Otyepka, *J. Phys. Chem. C*, 2016, **120**, 1303–1308.
29 M. A. Sk, A. Ananthanarayanan, L. Huang, K. H. Lim and P. Chen, *J. Mater. Chem. C*, 2014, **2**, 6954–6960.
30 S. Chen, N. Ullah, T. Wang and R. Zhang, *J. Mater. Chem. C*, 2018, **6**, 6875–6883.
31 M. Fu, F. Ehrat, Y. Wang, K. Z. Milowska, C. Reckmeier, A. L. Rogach, J. K. Stolarczyk, A. S. Urban and J. Feldmann, *Nano Lett.*, 2015, **15**, 6030–6035.
32 B. Shi, D. Nachtigallová, A. J. A. Aquino, F. B. C. Machado and H. Lischka, *Phys. Chem. Chem. Phys.*, 2019, **21**, 9077–9088.
33 L. Zdražil, Z. Baďura, M. Langer, S. Kalytchuk, D. Panáček, M. Scheibe, Š. Kment, H. Kmentová, M. A. Thottappali, E. Mohammadi, M. Medveď, A. Bakandritsos, G. Zoppellaro, R. Zbořil and M. Otyepka, *Small*, 2023, **19**, 2206587.
34 N. A. Romero and D. A. Nicewicz, *Chem. Rev.*, 2016, **116**, 10075–10166.
35 C. Butchosa, P. Guiglion and M. A. Zwijnenburg, *J. Phys. Chem. C*, 2014, **118**, 24833–24842.
36 A. W. Prentice and M. A. Zwijnenburg, *Adv. Energy Mater.*, 2021, **11**, 2100709.
37 J. Yi, W. El-Alami, Y. Song, H. Li, P. M. Ajayan and H. Xu, *Chem. Eng. J.*, 2020, **382**, 122812.
38 J. Wu, Z. Liu, X. Lin, E. Jiang, S. Zhang, P. Huo, Y. Yan, P. Zhou and Y. Yan, *Nat. Commun.*, 2022, **13**, 6999.
39 M. C. Scharber, D. Mühlbacher, M. Koppe, P. Denk, C. Waldauf, A. J. Heeger and C. J. Brabec, *Adv. Mater.*, 2006, **18**, 789–794.
40 N. Blouin, A. Michaud, D. Gendron, S. Wakim, E. Blair, R. Neagu-Plesu, M. Belletête, G. Durocher, Y. Tao and M. Leclerc, *J. Am. Chem. Soc.*, 2008, **130**, 732–742.
41 G. Dennler, M. C. Scharber and C. J. Brabec, *Adv. Mater.*, 2009, **21**, 1323–1338.
42 X. Liu, C. Huang and M. Li, *J. Phys. Chem. C*, 2016, **120**, 27148–27158.
43 L. Zhang, K. Pei, M. Yu, Y. Huang, H. Zhao, M. Zeng, Y. Wang and J. Gao, *J. Phys. Chem. C*, 2012, **116**, 26154–26161.
44 S.-B. Li, Y.-A. Duan, Y. Geng, H.-B. Li, J.-Z. Zhang, H.-L. Xu, M. Zhang and Z.-M. Su, *Phys. Chem. Chem. Phys.*, 2014, **16**, 25799–25808.
45 L. Zhu, Y. Yi and Z. Wei, *J. Phys. Chem. C*, 2018, **122**, 22309–22316.
46 T. M. Clarke and J. R. Durrant, *Chem. Rev.*, 2010, **110**, 6736–6767.
47 M. Ahn, M.-J. Kim and K.-R. Wee, *J. Org. Chem.*, 2019, **84**, 12050–12057.
48 A. V. Aksenov, S. V. Shcherbakov, I. V. Lobach, I. V. Aksenova and M. Rubin, *Eur. J. Org. Chem.*, 2017, 1666–1673.
49 T. M. Figueira-Duarte and K. Müllen, *Chem. Rev.*, 2011, **111**, 7260–7314.
50 S. Greßies, M. Ito, M. Sakai, H. Osaki, J. H. Kim, T. Gensch, C. Daniliuc, N. Ando, S. Yamaguchi and F. Glorius, *Chem. – Eur. J.*, 2021, **27**, 2753–2759.
51 J. Huang, J.-H. Sua and H. Tian, *J. Mater. Chem.*, 2012, **22**, 10977–10989.
52 A. Mukherjee, A. A. Akulov, S. Santra, M. V. Varaksin, G. A. Kim, D. S. Kopchuk, O. S. Taniya, G. V. Zyryanov and O. N. Chupakhin, *RSC Adv.*, 2022, **12**, 9323–9341.
53 I. Piskun, R. Blackwell, J. Jornet-Somoza, F. Zhao, A. Rubio, S. G. Louie and F. R. Fischer, *J. Am. Chem. Soc.*, 2020, **142**, 3696–3700.
54 V. Udumula, J. L. Endres, C. N. Harper, L. Jaramillo, H. A. Zhong, K. W. Bayles and M. Conda-Sheridan, *Eur. J. Med. Chem.*, 2017, **125**, 710–721.
55 Y. Wang, B. Liu, C. W. Koh, X. Zhou, H. Sun, J. Yu, K. Yang, H. Wang, Q. Liao, H. Y. Woo and X. Guo, *Adv. Energy Mater.*, 2019, **9**, 1803976.
56 M. J. Frisch, G. W. Trucks, H. B. Schlegel, G. E. Scuseria, M. A. Robb, J. R. Cheeseman, G. Scalmani, V. Barone, G. A. Petersson and H. Nakatsuji, *et al.*, *Gaussian 16, Revision C.01*, Gaussian, Inc., Wallingford CT, 2016.
57 M. Kubillus, T. Kubař, M. Gaus, J. Řezáč and M. Elstner, *J. Chem. Theory Comput.*, 2015, **11**, 332–342.
58 M. Gaus, A. Goez and M. Elstner, *J. Chem. Theory Comput.*, 2012, **9**, 338–354.
59 B. Hourahine, B. Aradi, V. Blum, I. S. Bonafé, A. Buccheri, C. Camacho, C. Cevallos, M. Y. Deshaye, T. Dumitrică, A. Dominguez, S. Ehlert, M. Elstner, T. van der Heide, J. Hermann, S. Irle, J. J. Kranz, C. Köhler, T. Kowalczyk, T. Kubař, I. S. Lee, V. Lutsker, R. J. Maurer, S. K. Min, I. Mitchell, C. Negre, T. A. Niehaus, A. M. N. Niklasson, A. J. Page, A. Pecchia, G. Penazzi, M. P. Persson, J. Řezáč, C. G. Sánchez, M. Sternberg, M. Stöhr, F. Stuckenberg, A. Tkatchenko, V. W.-z. Yu and T. Frauenheim, *J. Chem. Phys.*, 2020, **152**, 124101.
60 D. Van Der Spoel, E. Lindahl, B. Hess, G. Groenhof, A. E. Mark and H. J. C. Berendsen, *J. Comput. Chem.*, 2005, **26**, 1701–1718.
61 W. L. Jorgensen, D. S. Maxwell and J. Tirado-Rives, *J. Am. Chem. Soc.*, 1996, **118**, 11225–11236.
62 S.-Y. Kim, M.-J. Kim, M. Ahn, K.-M. Lee and K.-R. Wee, *Dyes Pigm.*, 2021, **191**, 109362.
63 C. Bannwarth and S. Grimme, *Comput. Theor. Chem.*, 2014, **1040**, 45–53.
64 S. Grimme, *J. Chem. Phys.*, 2013, **138**, 244104.

65 F. Neese, F. Wennmohs, U. Becker and C. Riplinger, *J. Chem. Phys.*, 2020, **152**, 224108.
66 F. Neese, *Wiley Interdiscip. Rev.:Comput. Mol. Sci.*, 2022, **12**, e1606.
67 A. V. Marenich, C. J. Cramer and D. G. Truhlar, *J. Phys. Chem. B*, 2009, **113**, 6378–6396.
68 F. Plasser, B. Thomitzni, S. A. Bäppler, J. Wenzel, D. R. Rehn, M. Wormit and A. Dreuw, *J. Comput. Chem.*, 2015, **36**, 1609–1620.
69 S. A. Bäppler, F. Plasser, M. Wormit and A. Dreuw, *Phys. Rev. A*, 2014, **90**, 052521.
70 F. Plasser, M. Wormit and A. Dreuw, *J. Chem. Phys.*, 2014, **141**, 024106.
71 F. Plasser, *J. Chem. Phys.*, 2020, **152**, 084108.
72 T. Le Bahers, C. Adamo and I. Ciofini, *J. Chem. Theory Comput.*, 2011, **7**, 2498–2506.
73 C. Adamo, T. Le Bahers, M. Savarese, L. Wilbraham, G. García, R. Fukuda, M. Ehara, N. Rega and I. Ciofini, *Coord. Chem. Rev.*, 2015, **304–305**, 166–178.
74 M. Isegawa, F. Neese and D. A. Pantazis, *J. Chem. Theory Comput.*, 2016, **12**, 2272–2284.
75 H. Neugebauer, F. Bohle, M. Bursch, A. Hansen and S. Grimme, *J. Phys. Chem. A*, 2020, **124**, 7166–7176.
76 Y. Fu, L. Liu, H.-Z. Yu, Y.-M. Wang and Q.-X. Guo, *J. Am. Chem. Soc.*, 2005, **127**, 7227–7234.
77 T. B. Demissie, K. Ruud and J. H. Hansen, *Organometallics*, 2015, **34**, 4218–4228.
78 S. M. Maley, G. R. Lief, R. M. Buck, O. L. Sydora, Q. Yang, S. M. Bischof and D. H. Ess, *J. Comput. Chem.*, 2023, **44**, 506–515.
79 D. Wang, S. Huang, C. Wang, Y. Yue and Q. Zhang, *Org. Electron.*, 2019, **64**, 216–222.
80 C. Adamo and D. Jacquemin, *Chem. Soc. Rev.*, 2013, **42**, 845–856.
81 A. A. Isse and A. Gennaro, *J. Phys. Chem. B*, 2010, **114**, 7894–7899.
82 W. R. Fawcett, *Langmuir*, 2008, **24**, 9868–9875.
83 N. Meng, J. Ren, Y. Liu, Y. Huang, T. Petit and B. Zhang, *Energy Environ. Sci.*, 2018, **11**, 566–571.
84 L. Li, S. Zhu, R. Hao, J.-J. Wang, E.-C. Yang and X.-J. Zhao, *Dalton Trans.*, 2018, **47**, 12726–12733.
85 S. Kang, M. He, M. Chen, Y. Liu, Y. Wang, Y. Wang, M. Dong, X. Chang and L. Cui, *ACS Appl. Mater. Interfaces*, 2019, **11**, 14952–14959.
86 L. S. Dodda, I. Cabeza de Vaca, J. Tirado-Rives and W. L. Jorgensen, *Nucleic Acids Res.*, 2017, **45**, W331–W336.
87 The PyMOL Molecular Graphics System, Version 3.0 Schrödinger, LLC.
88 D. van der Spoel, P. J. van Maaren and C. Caleman, *Bioinformatics*, 2012, **28**, 752–753.
89 C. Caleman, P. J. van Maaren, M. Hong, J. S. Hub, L. T. Costa and D. van der Spoel, *J. Chem. Theory Comput.*, 2012, **8**, 61–74.
90 B. Hess, H. Bekker, H. J. C. Berendsen and J. G. E. M. Fraaije, *J. Comput. Chem.*, 1998, **18**, 1463–1472.
91 H. J. C. Berendsen, J. P. M. Postma, W. F. van Gunsteren, A. DiNola and J. R. Haak, *J. Chem. Phys.*, 1984, **81**, 3684–3690.
92 G. Bussi, D. Donadio and M. Parrinello, *J. Chem. Phys.*, 2007, **126**, 014101.
93 T. Darden, D. York and L. Pedersen, *J. Chem. Phys.*, 1993, **98**, 10089–10092.
94 C. I. Bayly, P. Cieplak, W. Cornell and P. A. Kollman, *J. Phys. Chem.*, 1993, **97**, 10269–10280.